

Journal of Materials Chemistry A

Accepted Manuscript



This is an *Accepted Manuscript*, which has been through the Royal Society of Chemistry peer review process and has been accepted for publication.

Accepted Manuscripts are published online shortly after acceptance, before technical editing, formatting and proof reading. Using this free service, authors can make their results available to the community, in citable form, before we publish the edited article. We will replace this *Accepted Manuscript* with the edited and formatted *Advance Article* as soon as it is available.

You can find more information about *Accepted Manuscripts* in the [Information for Authors](#).

Please note that technical editing may introduce minor changes to the text and/or graphics, which may alter content. The journal's standard [Terms & Conditions](#) and the [Ethical guidelines](#) still apply. In no event shall the Royal Society of Chemistry be held responsible for any errors or omissions in this *Accepted Manuscript* or any consequences arising from the use of any information it contains.



Journal of Materials Chemistry A

Full Research Article

Highly Pseudocapacitive Nb-doped TiO₂ High Power Anodes for Lithium-ion Batteries

Mechthild Lübke^{a,b}, Juhun Shin^a, Peter Marchand^a, Dan Brett^c, Paul Shearing^c, Zhaolin Liu^b
and Jawwad A. Darr^{a*}

Received 00th January
20xx,
Accepted 00th January
20xx

DOI: 10.1039/x0xx00000x

www.rsc.org/

Nb-doped TiO₂ (anatase) nanoparticles were synthesized *via* a continuous hydrothermal flow synthesis reactor using a supercritical water flow as reagent and crystallizing medium. The as-prepared nano-powders with *ca.* 25 at% Nb⁵⁺ (< 6 nm diameter) were used as possible anodes for lithium-ion batteries without any further heat-treatment. Cyclic voltammetry and galvanostatic charge/discharge cycling tests were performed in the range of 1.2 to 3.0 V vs Li/Li⁺. The Nb-doped TiO₂ samples showed superior capacity retention at high current rates compared to the corresponding undoped nano-TiO₂. The superior performance of the doped samples (at specific currents up to 15 A g⁻¹) was attributed to higher electronic conductivity and a greater charge storage contribution from surface effects like pseudocapacitance (faradaic processes) and also some Helmholtz double layer.

^a Christopher Ingold Laboratories, Department of Chemistry, University College London, 20 Gordon Street, London, WC1H 0AJ, UK.

^b Institute of Materials Research and Engineering, Agency for Science, Technology and Research (A*STAR), 3 Research Link, Singapore 117602, Singapore.

^c Department of Chemical Engineering, University College London, Torrington Place, London, WC1E 7JE, U.K.

* Corresponding author: Prof. Jawwad A. Darr, email: j.a.darr@ucl.ac.uk

Journal of Materials Chemistry A

Full Research Article

Introduction

Lithium-ion batteries are widely used as the main power source for portable electronics such as mobile phones and handheld devices. Developments in consumer electronics and the need to reduce CO₂ emissions in cities has led to interest in the use of Li-ion batteries in electric vehicles¹. The typical design of a Li-ion battery consists of a Li-ion containing cathode (e.g. lithium iron phosphate), an anode (e.g. graphitic carbons), an organic electrolyte (containing Li-ion salt), and an ion-conductive separator to physically separate the two electrodes². The charge/discharge process is referred to the reversible electrochemical process of ions moving across the positive and negative electrodes, which allows storage and release of charge in form of electrical energy.

Because of their high surface area to volume ratio, nanomaterials are of interest as Li-ion battery electrodes. The greater proportion of electrically charged species nearer to the surface (compared to bulk materials) can aid faster electronic/ion transfer processes. This can facilitate charge storage in electrodes *via* surface effects (i.e. not exclusively from Li-ion intercalation/insertion)³. For example, fast faradaic reactions (pseudocapacitive effects) of Li-ions at the extensive surfaces can enhance charge storage at higher current rates⁴. Additionally, a high surface area nanomaterial can behave like an electrochemical double layer capacitor, in which the charge is stored physically *via* a Helmholtz double layer. Hence, overall storage in nanomaterial electrodes such as nano-TiO₂⁴⁻⁸ and nano-Nb₂O₅⁹⁻¹¹, can be a combination of (i) battery-like Li-ion insertion/intercalation and (ii) supercapacitor-like charge arising from either faradaic redox reactions at the surface¹² and Helmholtz double layer charge transfer.

Titanium dioxide is an ideal electrode material to replace graphite as it is inexpensive, environmentally friendly and stable in a wide range of temperature and pH conditions. In comparison to TiO₂, graphite suffers from low power density issues and requires a protective solid electrolyte interface layer to be formed^{4-7, 13-17}. Moreover, TiO₂ as an anode offers low irreversible capacity loss and

has a structure that is stable under long term charge/discharge cycling across a range of C-rates, including very high rates. Although the theoretical capacity of TiO₂ is relatively low compared to some other anode materials (theoretical capacities of Li-metal, Si, Sn, graphite and TiO₂ are 3860, 4200, 993, 372, and 335 mAh g⁻¹, respectively), TiO₂ can offer better performance at higher power. Furthermore, alloy materials undergo very large volume expansions during lithiation and delithiation processes and, therefore, they can experience relatively high irreversible capacity losses due to changes in electrode structure^{2, 18-20}.

Unmodified TiO₂ (anatase) anodes possess low electronic conductivity due to a wide band gap (ca. 3.0 to 3.4 eV)²¹. However, it is possible to increase this *via* introduction of dopants (such as Nb⁵⁺) into the structure^{7, 15, 16, 22}. Recently, Fehse *et al.* showed that the partial density of states (PDOS) of Nb 4d and Ti 3d are similar, but the additional Nb 4d electron pushes the Fermi level from the top of the valence band for undoped TiO₂ to the bottom of the conduction band for Nb-doped TiO₂. The lowest Nb 4d empty states are not in the band gap, but overlap with Ti 3d empty states to form a band in the range 0 to 2 eV. As the Fermi level is located within this band, Nb-doped anatase TiO₂ exhibits metallic conductivity due to the delocalization of this additional Nb 4d electron¹⁶.

High power Nb₂O₅ based anodes have received much attention due to their ability to rapidly store charge from a combination of Li-ion intercalation / deintercalation and pseudocapacitive charge storage^{10, 11, 23-25}. DFT analysis has suggested that strong lithium-ion adsorption at the surface of NbO_x (where x = 1.3, 1.6 or 2), contributes to the observed high rate performance. Therefore, in this case, the presence of local charge transfer at adsorption sites drastically increases the energy density⁹.

In this work, the direct and continuous synthesis of undoped nano-TiO₂ (anatase) and nanosized Nb-doped TiO₂ (up to 25 at% dopant) is reported. The incorporation of Nb⁵⁺ in the structure improves the electrochemical performance (compared to undoped nano-TiO₂) at

higher charge/discharge rates. The results are described in terms of the impact of doping on electronic conductivity, Li-ion diffusion kinetics and charge storage properties (*via* diffusion controlled and surface effects) on timescales of a few minutes or a few seconds.

Experimental

Materials

TIBALD (Titanium(IV) bis(ammonium lactato)dihydroxide solution, 50% H₂O, Sigma Aldrich, Steinheim, Germany), ammonium niobate (V) oxalate hydrate (Sigma-Aldrich, >99.99%, Steinheim, Germany) and KOH (Fisher Scientific, Loughborough, UK) were used as aqueous precursors in D.I. Water (10 M Ω).

Synthesis

The nanoparticles were synthesized using a laboratory scale continuous hydrothermal flow synthesis (CHFS) reactor incorporating a confined jet mixer (CJM), the basic design of which is described elsewhere²⁶⁻²⁸. The laboratory scale process is similar to the pilot plant CHFS process described elsewhere^{29,30} but on *ca.* 1/5 of the scale. In the lab scale process, three identical diaphragm pumps (Primeroyal K, Milton Roy, Pont-Saint-Pierre, France) were used to supply three feeds, which were pressurized to 24.1 MPa. Pump 1 supplied a feed of DI water at a flow rate of 80 mL min⁻¹, which was then heated above the critical point of water ($T_c = 374^\circ\text{C}$ and $P_c = 22.1$ MPa) in flow using a 7 kW electrical water heater. Pump 2 supplied the metal salt (precursor 1) at a flow rate of 40 mL min⁻¹ and pump 3 supplied either auxiliary reagents (precursor 2) or DI water at a flow rate of 40 mL min⁻¹. The feeds from pumps 2 and 3 were combined at room temperature in a dead volume tee-piece. This precursor mixture was then brought into contact (co-currently) with the flow of supercritical water in a CJM (patent application no. GB1008721).

For the synthesis of undoped TiO₂, 0.3 M TiBALD was used as metal salt precursor 1 and DI water was used in place of precursor 2. DI water from pump 1 was heated to 400 °C and mixed with the combined precursor feed, resulting in a calculated reaction temperature of 305 °C inside the CJM.

For the synthesis of Nb-doped TiO₂, 0.4 M TiBALD and 0.1 M ammonium niobate (V) oxalate hydrate were premixed at room temperature and used as metal salt precursor 1. This mixture was

then combined in flow with 0.3 M KOH (precursor 2) in the tee-piece (as part of the CHFS process). This combined precursor feed (metal salt + base) was mixed with the supercritical water flow (heated to 450 °C) to give a calculated mixing temperature of 335 °C in the CJM.

The residence time for both the undoped and doped nanomaterials that formed in the mixer was *ca.* 5 s, before the start of the pipe-on-pipe cooler which is part of the CHFS process. The particle-laden flow was cooled to ~40°C, whereupon it passed through a back-pressure regulator (BPR) and was collected. More details of the synthesis method can be found in the Supplementary Information.

The resulting nanoparticle-laden slurry was cleaned by allowing the solids to settle before washing with DI water and then freeze-dried (Virtis Genesis 35XL) by cooling to -60 °C, followed by slow heating under vacuum of <100 mTorr over a period of 24 h. The dried powders were used directly for preparation as electrode inks with no further processing.

Characterization

Powder X-ray diffraction (XRD) patterns of the samples were obtained on a STOE diffractometer using Mo-K α radiation ($\lambda = 0.71$ Å) over the 2θ range 7 to 40° with a step size of 0.5° and step time of 30 s. X-ray photoelectron spectroscopy (XPS) measurements were collected using a Thermo Scientific™ K-alpha™+ spectrometer using Al-K α radiation and a 128-channel position sensitive detector. Survey scans were conducted at a pass energy of 150 eV and high resolution scans were conducted at a pass energy of 50 eV for Ti(2p), Nb(3d), O(1s) and C(1s). The XPS spectra were processed using CasaXPS™ software (version 2.3.16) and the binding energy scales were calibrated using the adventitious C 1s peak at 284.5 eV. Backgrounds were subtracted using the Shirley routine³¹ and peaks were fitted with an appropriate Gaussian/Lorentzian line shape. Relative concentrations of Ti and Nb within the sample were estimated by measurement of the peak areas of Ti(2p) and Nb(3d) core lines and application of the appropriate relative sensitivity factors. Full details of this analysis can be found in the Supplementary Information.

The size and morphology of the crystallites were determined by transmission electron microscopy (TEM) using a Jeol JEM 2100 – LaB₆ filament. The system was equipped with a Gatan Orius digital

camera for digital image capturing. Samples were prepared by ultrasonically dispersing a few mg of the powder in ethanol (>99.5%, EMPLURA, Darmstadt, Germany) and pipetting drops of the dispersed sample on to a copper film grid (300 mesh – Agar Scientific, Stansted, UK). The average crystallite size was determined by the average of at least 60 crystallites. Brunauer-Emmett-Teller (BET) surface area measurements were carried out using N₂ in a micrometrics ASAP 2020 machine. Prior to analysis, the samples were degassed at 150 °C (12 h) under vacuum before measurements.

Electrochemical Characterization

The freeze-dried nanomaterials were used as electrode active materials without any further processing or treatments. The slurry for the electrode was prepared with a content of 70 wt% active material, 20 wt% conductive agent (carbon black, Super P, Alfa Aesar, Heysham, UK) and 10 wt% polyvinylidene fluoride, PVDF, (PI-KEM, Staffordshire, UK). PVDF was dissolved in NMP (N-methyl-2-pyrrolidone, Sigma Aldrich, St. Louis, USA) for at least 1 hour at room temperature, before adding the active material and conductive agent. The mixtures were milled and the slurry was cast on a copper foil (PI-KEM, Staffordshire, UK) and dried in an oven at 70 °C for 1 hour and then left overnight at room temperature. Electrodes with a diameter of 16 mm were punched out, pressed and finally dried overnight at 70 °C. The specific electrode mass loading for each electrode disc with a diameter of 16 mm was in the range of 1.0 to 1.5 mg cm⁻². Electrochemical experiments were performed using a two-electrode 2032-type coin cell, which was assembled in an argon-filled glovebox with O₂ and H₂O limited below 50 ppm. The counter electrode was lithium metal foil (PI-KEM, Staffordshire, UK). The separator (glass microfiber filters, WHATMAN, Buckinghamshire, UK) was saturated with an organic electrolyte of LiPF₆ in 3:7 wt% ethylene carbonate/ethyl methyl carbonate (BASF, Ludwigshafen, Germany).

Electrochemical measurements were performed using a 48-channel Arbin Instrument (Caltest Instruments Ltd, Guildford, UK) at room temperature. The electrochemical performance was first investigated by cyclic voltammetry (CV) in the potential range 1.2 to 2.5 V vs Li/Li⁺ with the scan rate in the range 0.05 mV s⁻¹ to 1 mV s⁻¹. The specific current rate test was performed between an applied current in the range 0.1 to 15 A g⁻¹ in the potential range of 1.2 to 3 V vs Li/Li⁺. The specific current and specific capacity was

calculated based on the mass of active material in each printed electrode and 1C corresponded to a theoretical specific capacity of 175 mAh g⁻¹.

Electrochemical impedance spectroscopy (EIS) was measured by applying an AC (alternating current) potential (5 mV) across a frequency range of 10 mHz to 500 kHz to an electrochemical cell and then measuring the current response through the cell with a galvanostat/potentiostat (PGSTAT302, AUTOLAB, Metrohm). The cell was assembled with Celgard 2400 separator soaked with 1 M LiPF₆ in EC/DMC/DEC (1:1:1, v/v) as electrolyte with a lithium metal counter electrode for this measurement.

Results and discussion

Undoped TiO₂ and Nb-doped TiO₂ were obtained as white and blue powders, respectively (see Figure 1a). The reaction yield in each case was >90%. The XRD data confirmed a good match to the pattern for phase pure anatase TiO₂ (tetragonal, space group I4₁/amd, JCPDS 21-1272), see Figure 1b. High-quality XRD data revealed very minor impurity peaks in the Nb-doped TiO₂ sample at 2θ = 14.4 and 20.5°. The peak at 2θ = 14.4 ° might be attributed to the (100) peak of a very small amount of pseudo-hexagonal TT-Nb₂O₅ (JCPDS 28-317)¹⁰ although the other peak did not correspond to any possible Nb₂O₅ phase. Therefore, the two impurity peaks most likely corresponded to the (211) and (302) peaks of a very minor brookite phase (similar to JCPDS reference pattern 29-1360). Another indication for a brookite impurity was the slight shoulder of the first peak at ca. 13° which might be attributed to the (111) brookite peak. There was a small shift to lower 2θ values for the peaks of the Nb-doped TiO₂ compared to the undoped counterpart at higher angles. This was due to lattice expansion, resulting from the substitution of larger Nb⁵⁺ (ionic radius = 0.64 Å) for Ti⁴⁺ (ionic radius = 0.61 Å) in the anatase structure (TiO₆ octahedra). The calculated Scherrer crystallite sizes were ca. 4.3 and 5.0 nm for the undoped and Nb-doped TiO₂, respectively, which was comparable to the sizes of previously reported TiO₂ based materials made *via* CHFS³²⁻³⁵.

The valence state of the metal ions was determined with X-ray photoelectron spectroscopy (XPS) [see Figure 2]. The Nb-3d level binding energies were 210.65 eV (Nb 3d_{5/2}) and 207.91 eV (Nb 3d_{3/2}) with a spin orbit splitting of 2.74 eV, which were assigned to

the core levels of Nb⁵⁺. The Ti-2p level binding energies were 464.92 eV (Ti 2p_{1/2}) and 459.15 eV (Ti 2p_{3/2}) with a spin orbit splitting of 5.77 eV, which were assigned to the core levels of Ti⁴⁺. No additional Ti peaks were observed within the spectra, suggesting that Ti⁴⁺ was the only Ti species present. Semi-quantitative analysis of the peak areas for the Ti(2p) and Nb(3d) core lines estimated the elemental composition at the surface to be 25 at% Nb relative to Ti. It is noted, however, that such analysis is relevant only for the surface of the sample and can be subject to errors arising from ineffective background subtraction and potential sample inhomogeneity³⁶. Corroboratory compositional analysis was therefore obtained by EDX measurements, giving values of 22.6 ± 1.9 at% Nb relative to Ti. These results corresponded well to the value estimated by XPS, as well as the precursor concentration used in the synthesis, suggesting that the Nb dopant was effectively and homogeneously incorporated into the TiO₂ structure.

TEM images revealed very small spherical particles with narrow size distribution for both undoped and Nb-doped titania (Figure 3 for doped sample). The average crystallite size of undoped and Nb-doped TiO₂ was 4.5 (±0.6) and 4.9 (±0.6) nm, respectively, which was in agreement with the trends of the BET surface area. The interlayer spacing for undoped and doped TiO₂ was calculated from relevant TEM images and was found to be 0.34 (±0.02) and 0.34 (±0.01) nm, respectively, which is consistent with expectations for the (101) planes of tetragonal-phase anatase. STEM/EDX mapping confirmed a homogenous distribution of Ti and Nb atoms in the sample (Figure 3c and Figure 3d, respectively). The BET surface area of the undoped TiO₂ was 288 m² g⁻¹ and of Nb-doped TiO₂ was 239 m² g⁻¹.

Cyclic voltammograms under different conditions were carried out to gain a better understanding of the electrochemical performance of these two materials. The specific current response at an applied scan rate of 1 mV s⁻¹ is presented in Figure 4a. A decrease in peak height was observed with doping of 25 at% Nb into TiO₂ in the characteristic range where Ti³⁺/Ti⁴⁺ is active (1.6 and 2.2 V vs Li/Li⁺, respectively). Interestingly, the peak potential for undoped titania exhibited a higher peak shift (difference between the lithiation and delithiation peaks) of 0.52 V compared to the Nb-doped material (peak shift 0.47 V). This gave an indirect indication of better Li-ion insertion kinetics for the Nb-doped TiO₂^{37, 38}, which could be a

consequence of a slightly higher interlayer spacing expected for the Nb-doped sample (compared to the undoped TiO₂). Two further peaks were observed for the Nb-doped TiO₂ at 1.49 and 1.67 V vs Li/Li⁺ for the lithiation and delithiation, respectively. These might be attributed to the reduction of Nb⁵⁺ and oxidation of Nb⁴⁺ back to Nb⁵⁺^{11, 23}.

A scan rate test was carried out to distinguish the charge stored *via* diffusion-controlled Li-ion insertion from surface effects (Figure 4b). In general, the current in a scan rate experiment can be expressed by a power law (equation 1), where *i* is the current (A), *a* and *b* are arbitrary coefficients and *v* is the potential scan rate (V s⁻¹).

$$i = av^b \quad (1)$$

The coefficient *b* can be expected to vary in the range 0.5 to 1.0, with a value of 0.5 being characteristic of a diffusion-limited process (charge storage *via* Li-ion insertion) and a value of 1.0 for a capacitive process (charge storage *via* surface capacitive effects). Therefore, to further quantify the different charge storage mechanisms, charge storage *via* Li-ion insertion and surface capacitive effects were separated out, using a method that has been described previously in the literature^{5, 10-12}. At a fixed potential, the current response can be seen as a combination of the two aforementioned charge storage mechanisms. The surface capacitive effect (fast kinetics) can be expressed by *k*₁*v* (*b* = 1.0), whereas the diffusion-controlled (Li-ion insertion) contribution can be expressed by *k*₂*v*^{1/2} (*b* = 0.5) (equation 2).

$$i_E = k_1v + k_2v^{1/2} \quad (2)$$

$$i_E/v^{1/2} = k_1v^{1/2} + k_2 \quad (3)$$

At a certain potential, the current value was measured for each scan rate. A plot of *i*_E/*v*^{1/2} versus *v*^{1/2}, allowed the calculation of *k*₂ from the y-intercept, and *k*₁ from the slope of equation 3. The slight shift of the Li-ion de-/insertion peak for higher applied sweep rates was ignored and the potential value from a sweep rate of 0.5 mV s⁻¹ was used as the standard de-/insertion potential. Low scan rates (range of 0.05 to 1 mV s⁻¹) were chosen as the peak shifted more at higher applied rates⁵. The calculated *k*₂ value was then used to quantify the amount of charge stored *via* surface capacitance at each potential. In this work, the current that

resulted from capacitive effects at the surface was calculated at a scan rate of 0.5 mV s^{-1} , which was then plotted against the overall measured current (as shown in Figures 4c and 4d). The calculated current response arising from capacitive effects at the surface was then deduced (grey areas in Figures 4c and 4d). It can be seen that the grey area in Figure 4d was larger for the Nb-doped sample than the undoped sample (Figure 4c), particularly in the range 1.4 to 1.7 V vs Li/Li⁺. This was due to the presence of the near surface Nb-dopant, as suggested previously^{10, 23, 25, 39-42}. Thus, calculation of the areas, as described above, enabled approximate quantification of the relative contributions from charge stored *via* capacitive (pseudocapacitance and Helmholtz double layer charge) and diffusion-limited processes (*i.e.* classical Li-ion insertion). Undoped TiO₂ showed charge storage contributions *via* capacitance and conventional Li-ion insertion to be *ca.* 50% each (scan rate 0.5 mV s^{-1}). In contrast, Nb-doped TiO₂ showed charge storage contributions of *ca.* 65% *via* capacitance and 35% *via* diffusion-limited Li-ion insertion processes (scan rate 0.5 mV s^{-1}), respectively. In comparison, Wang *et al.* previously made similar investigations on undoped titania at this scan rate, and found that capacitance accounted for *ca.* 55% of the capacity⁵.

Overall, the charge storage behavior shown in Figure 4c and Figure 4d fitted well to the galvanostatic charge/discharge cycling results (Figure 5a). Diffusion-limited charge storage processes are expected to decrease drastically when the electrode material is electrochemically cycled within seconds, as the main charge storage mechanism is due to surface effects at these high rates. As shown in Figure 5a, galvanostatic cycling tests at different specific current rates were performed in a wide current range from 0.1 to 15 A g^{-1} (considering $1\text{C} = 175 \text{ mAh g}^{-1}$, this is equivalent to a C-rate range of *ca.* 0.5C to 86C). It should be mentioned that the C-rate corresponds to the full theoretical charge/discharge within one hour for 1C, but this relates to the bulk de-/lithiation charge storage mechanism, which is typical for a battery material. The materials presented herein showed significant charge storage *via* surface effects, which are more commonly associated with oxide supercapacitors. Therefore, the authors prefer to use the term "nominal C-rate" hereafter and will also name each measured time for charge/discharge at each rate.

At the lowest applied current rate, the undoped and Nb-doped TiO₂ showed a specific capacity of 186 mAh g^{-1} and 180 mAh g^{-1} , respectively (nominal C-rate *ca.* 0.5C, 6200 s per charge or discharge). At higher currents, the Nb-doped TiO₂ showed superior rate retention when compared to its undoped counterpart; at a current rate of 5 A g^{-1} (nominal C-rate *ca.* 29C, 65 s per charge or discharge), the undoped and Nb-doped TiO₂ showed a specific capacity of 88 mAh g^{-1} and 105 mAh g^{-1} , respectively. At the highest applied current of 15 A g^{-1} (nominal C-rate *ca.* 86C, 10 s per charge or discharge), the undoped and doped nano-TiO₂ samples showed a specific capacity of 27 and 48 mAh g^{-1} , respectively.

The potential versus capacity plot suggested that the overpotential between lithiation and delithiation (current rate 5 A g^{-1}) was higher for the undoped TiO₂ compared to the Nb-doped TiO₂ (Figure 5b), which suggested higher electronic conductivity for the Nb-doped sample. As this can often be a limiting factor for high power electrode materials⁴³, it explains the better performance of the doped sample. Long-term galvanostatic charge/discharge cycling for the Nb-doped sample is presented in Figure 5c (specific current rate 0.5 A g^{-1}). The coulombic efficiency remained >98.7 % and overall a specific capacity retention of *ca.* 91% (initial and final value 168 and 153 mAh g^{-1} , respectively) was achieved after 540 cycles. Therefore, the as-prepared nano-sized Nb-doped TiO₂ showed very high cycle stability at a modest current rate of 0.5 A g^{-1} .

Electrochemical impedance spectroscopy (EIS) were performed in order to further investigate the improved performance of Nb-doped TiO₂ at higher rates (Figure 5d). The EIS results were similar for both samples and each curve was divided into a high frequency region (a semicircle) and a low frequency region (a straight line). The high-frequency intercept with the real axis represents the ohmic resistance, which is related to the electrolyte and therefore, in the same range for both samples (as they were both measured under the same conditions). The semicircle at higher frequencies gives some information about the electrode resistance (charge-transfer resistance). As shown in the Nyquist plot in Figure 5d, the general trend was towards lower resistance for the doped sample (41Ω) versus the undoped sample (62Ω). This suggested higher electronic conductivity, which has been previously observed for Nb-doped titanium oxides^{16, 44, 45}.

Interestingly, the results herein suggested that the BET surface area was not the most critical parameter for the high power performance. Although the BET surface area decreased with higher Nb-dopant level, the overall stored charge increased. This has been observed previously with both Nb₂O₅¹⁰ and MnO₂⁴⁶ anode materials. Therefore, the combined effect of higher electronic conductivity, improved lithium-ion kinetics and higher capacity for charge storage *via* surface effects benefitted the high power performance for nanosized Nb-doped TiO₂ compared to the undoped material. As other transition metal oxides are known to show very promising high power performances due to faradaic processes, future studies will investigate the effect of alternative dopants (*e.g.* Ru, Mn, Fe, Ni, *etc.*) in nano-TiO₂ and other host systems⁴⁷.

Conclusions

This work reports the direct and continuous synthesis of high surface area anatase undoped TiO₂ and Nb-doped TiO₂ nanoparticles. Doping 25 at% Nb⁵⁺ into the anatase TiO₂ drastically improved the electrochemical performance at higher charge/discharge rates. The improved high power performance of the Nb-doped TiO₂ was attributed to its higher electronic conductivity, higher lithium-ion diffusivity and increased charge stored *via* surface effects. Overall, the direct synthesis of high power doped/undoped anode nanomaterials has been demonstrated and this CHFS process holds potential for further materials development and even scale-up production in the future. The authors hope to develop these areas further and the results of such endeavors will be reported in due course.

Acknowledgements

The EPSRC are thanked for funding the Centre for Doctoral Training in Molecular Modelling & Materials Science (UCL, UK) and A Star (Singapore) are thanked for supporting a studentship for ML. Mr Joe Nolan (UCL) is thanked for technical support. Dr Chris Tighe and Dr Rob Gruar are acknowledged for their contributions towards development of the lab scale CHFS process, which was used in this work. JAD, DB and PS thank EPSRC for support of the ELEVATE (ELEctrochemical Vehicle Advanced TEchnology) low carbon vehicles project (EP/M009394/1).

References

1. Z. Juda, *Journal of KONES*, 2011, **18**, 165-171.
2. M. Winter and R. J. Brodd, *Chemical reviews*, 2004, **104**, 4245-4270.
3. P. Simon, Y. Gogotsi and B. Dunn, *Science Magazine*, 2014, **343**, pp. 1210-1211.
4. K. Zhu, Q. Wang, J.-H. Kim, A. A. Pesaran and A. J. Frank, *The Journal of Physical Chemistry C*, 2012, **116**, 11895-11899.
5. J. Wang, J. Polleux, J. Lim and B. Dunn, *The Journal of Physical Chemistry C*, 2007, **111**, 14925-14931.
6. L. Wu, D. Buchholz, D. Bresser, L. Gomes Chagas and S. Passerini, *Journal of Power Sources*, 2014, **251**, 379-385.
7. H. Usui, S. Yoshioka, K. Wasada, M. Shimizu and H. Sakaguchi, *ACS Applied Materials & Interfaces*, 2015, **7**, 6567-6573.
8. M. Lübke, I. Johnson, N. M. Makwana, D. Brett, P. Shearing, Z. Liu and J. A. Darr, *Journal of Power Sources*, 2015, **294**, 94-102.
9. A. A. Lubimtsev, P. R. Kent, B. G. Sumpter and P. Ganesh, *Journal of Materials Chemistry A*, 2013, **1**, 14951-14956.
10. J. W. Kim, V. Augustyn and B. Dunn, *Advanced Energy Materials*, 2012, **2**, 141-148.
11. V. Augustyn, J. Come, M. A. Lowe, J. W. Kim, P.-L. Taberna, S. H. Tolbert, H. D. Abruña, P. Simon and B. Dunn, *Nature materials*, 2013, **12**, 518-522.
12. V. Augustyn, P. Simon and B. Dunn, *Energy & Environmental Science*, 2014, **7**, 1597-1614.
13. Y. S. Hu, L. Kienle, Y. G. Guo and J. Maier, *Advanced Materials*, 2006, **18**, 1421-1426.
14. S. Hu, H. Wang, J. Cao, J. Liu, B. Fang, M. Zheng, G. Ji, F. Zhang and Z. Yang, *Materials Letters*, 2008, **62**, 2954-2956.
15. Y. Wang, B. M. Smarsly and I. Djerdj, *Chemistry of Materials*, 2010, **22**, 6624-6631.
16. M. Fehse, S. Cavaliere, P. E. Lippens, I. Savych, A. Iadecola, L. Monconduit, D. J. Jones, J. Rozière, F. Fischer, C. Tessier and L. Stievano, *The Journal of Physical Chemistry C*, 2013, **117**, 13827-13835.
17. J. Qiu, S. Li, E. Gray, H. Liu, Q.-F. Gu, C. Sun, C. Lai, H. Zhao and S. Zhang, *The Journal of Physical Chemistry C*, 2014, **118**, 8824-8830.
18. S. Goriparti, E. Miele, F. De Angelis, E. Di Fabrizio, R. Proietti Zaccaria and C. Capiglia, *Journal of Power Sources*.
19. M. R. Palacin, *Chemical Society Reviews*, 2009, **38**, 2565-2575.
20. W.-J. Zhang, *Journal of Power Sources*, 2011, **196**, 13-24.
21. A. G. Dylla, G. Henkelman and K. J. Stevenson, *Accounts of Chemical Research*, 2013, **46**, 1104-1112.
22. J.-H. Jeong, D.-w. Jung, E. W. Shin and E.-S. Oh, *Journal of Alloys and Compounds*, 2014, **604**, 226-232.
23. M. Wei, K. Wei, M. Ichihara and H. Zhou, *Electrochemistry Communications*, 2008, **10**, 980-983.
24. P. Poizot, S. Laruelle, S. Grugeon, L. Dupont and J. M. Tarascon, *Nature*, 2000, **407**, 496-499.
25. J. Come, V. Augustyn, J. W. Kim, P. Rozier, P.-L. Taberna, P. Gogotsi, J. W. Long, B. Dunn and P. Simon, *Journal of The Electrochemical Society*, 2014, **161**, A718-A725.
26. J. A. Darr and M. Poliakoff, *Chemical Reviews*, 1999, **99**, 495-542.
27. R. I. Gruar, C. J. Tighe and J. A. Darr, *Industrial & Engineering Chemistry Research*, 2013, **52**, 5270-5281.

28. M. Lübke, N. M. Makwana, R. Gruar, C. Tighe, D. Brett, P. Shearing, Z. Liu and J. A. Darr, *Journal of Power Sources*, 2015, **291**, 102-107.
29. M. Chen, C. Y. Ma, T. Mahmud, J. A. Darr and X. Z. Wang, *The Journal of Supercritical Fluids*, 2011, **59**, 131-139.
30. C. J. Tighe, R. Q. Cabrera, R. I. Gruar and J. A. Darr, *Industrial & Engineering Chemistry Research*, 2013, **52**, 5522-5528.
31. D. S. H.-r. X-ray, *Rev. B*, 1972, **5**, 4709-4714.
32. Z. Zhang, S. Brown, J. B. Goodall, X. Weng, K. Thompson, K. Gong, S. Kellici, R. J. Clark, J. R. Evans and J. A. Darr, *Journal of Alloys and Compounds*, 2009, **476**, 451-456.
33. X. Li, Y. Qiu, S. Wang, S. Lu, R. I. Gruar, X. Zhang, J. A. Darr and T. He, *Physical Chemistry Chemical Physics*, 2013, **15**, 14729-14735.
34. J. B. Goodall, S. Kellici, D. Illsley, R. Lines, J. C. Knowles and J. A. Darr, *RSC Advances*, 2014, **4**, 31799-31809.
35. Z. Zhang, J. B. Goodall, D. J. Morgan, S. Brown, R. J. Clark, J. C. Knowles, N. J. Mordan, J. R. Evans, A. F. Carley and M. Bowker, *Journal of the European Ceramic Society*, 2009, **29**, 2343-2353.
36. P. Van der Heide, *X-ray photoelectron spectroscopy: an introduction to principles and practices*, John Wiley & Sons, 2011.
37. B. Hao, Y. Yan, X. Wang and G. Chen, *ACS applied materials & interfaces*, 2013, **5**, 6285-6291.
38. J. Wang, Y. Zhou, Y. Hu, R. O'Hayre and Z. Shao, *Journal of Materials Science*, 2013, **48**, 2733-2742.
39. M. Wei, Z.-m. Qi, M. Ichihara and H. Zhou, *Acta Materialia*, 2008, **56**, 2488-2494.
40. H. Luo, M. Wei and K. Wei, *Materials Chemistry and Physics*, 2010, **120**, 6-9.
41. H. Wen, Z. Liu, J. Wang, Q. Yang, Y. Li and J. Yu, *Applied Surface Science*, 2011, **257**, 10084-10088.
42. A. Le Viet, M. V. Reddy, R. Jose, B. V. R. Chowdari and S. Ramakrishna, *Electrochimica Acta*, 2011, **56**, 1518-1528.
43. P. V. Braun, J. Cho, J. H. Pikul, W. P. King and H. Zhang, *Current Opinion in Solid State and Materials Science*, 2012, **16**, 186-198.
44. B. Tian, H. Xiang, L. Zhang, Z. Li and H. Wang, *Electrochimica Acta*, 2010, **55**, 5453-5458.
45. S. Lee, J. H. Noh, H. S. Han, D. K. Yim, D. H. Kim, J.-K. Lee, J. Y. Kim, H. S. Jung and K. S. Hong, *The Journal of Physical Chemistry C*, 2009, **113**, 6878-6882.
46. O. Ghodbane, J.-L. Pascal and F. Favier, *ACS applied materials & interfaces*, 2009, **1**, 1130-1139.
47. P. Simon and Y. Gogotsi, *Nat Mater*, 2008, **7**, 845-854.

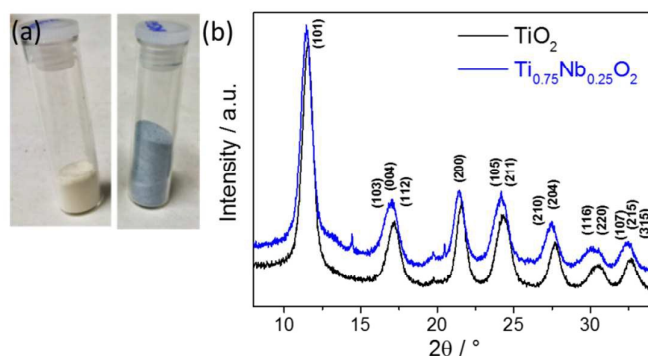


Figure 1: (a) Photograph of the pure (left) and doped (right) dried powder. (b) XRD patterns of pure (bottom, black) and Nb-doped anatase TiO₂ (top, blue).

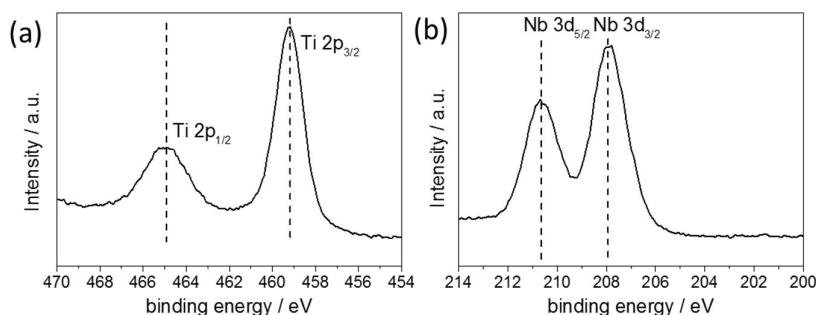


Figure 2: XPS spectra for the doped sample: high-resolution (a) Ti 2p and (b) Nb 3d spectra.

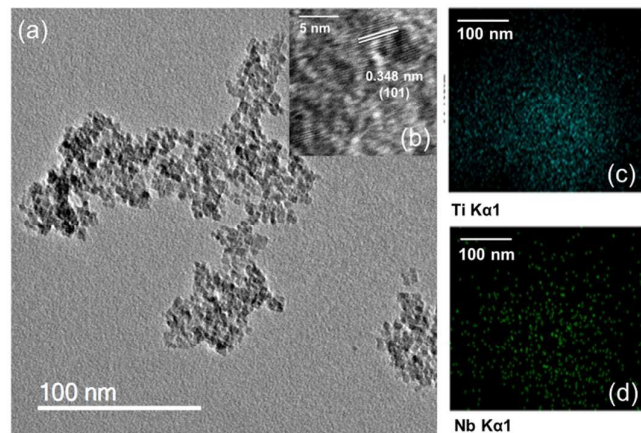


Figure 3: (a) and (b) HRTEM images of $\text{Ti}_{0.75}\text{Nb}_{0.25}\text{O}_2$. EDX mapping of $\text{Ti}_{0.75}\text{Nb}_{0.25}\text{O}_2$ showing the homogeneously distribution of (c) Ti and (d) Nb atoms.

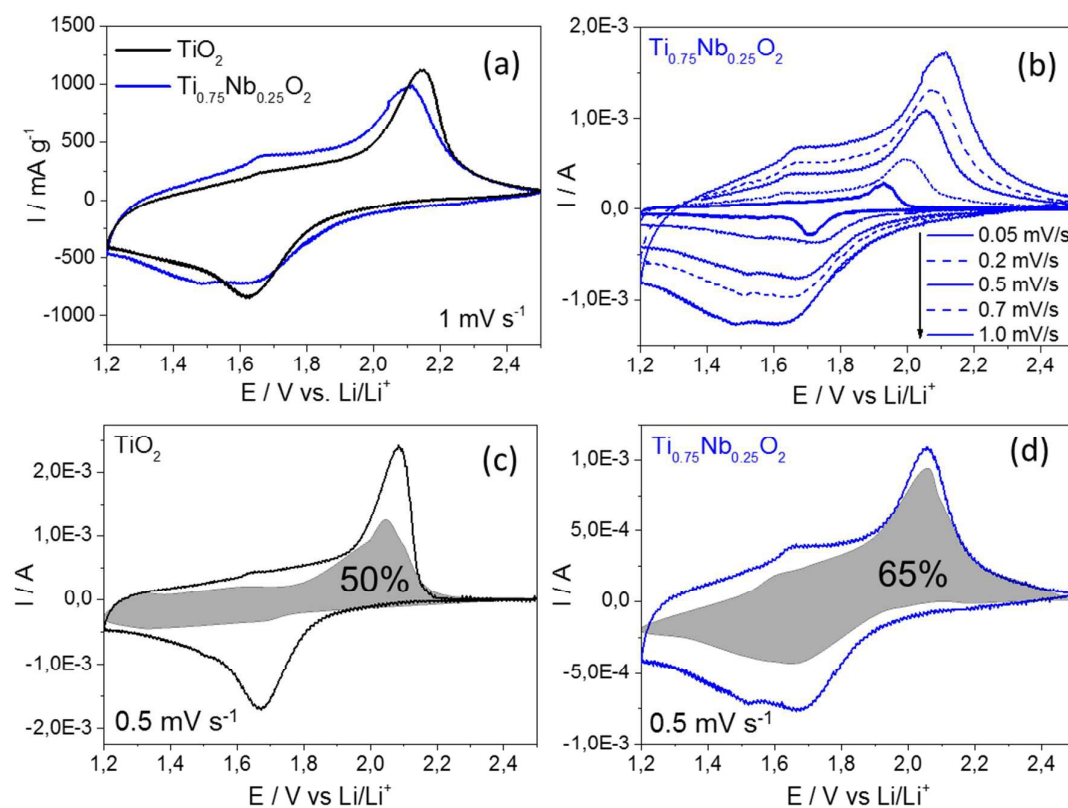


Figure 4: Cyclic voltammograms of the doped and undoped titanias (a) at an applied scan rate of 1 mV s^{-1} , (b) at applied rates in the range of 0.05 to 1 mV s^{-1} (scan rate test). The calculated current response arising from charge storage *via* capacitance (grey area) at a scan rate of 0.5 mV s^{-1} is shown for (c) pure TiO_2 and (d) $\text{Ti}_{0.75}\text{Nb}_{0.25}\text{O}_2$.

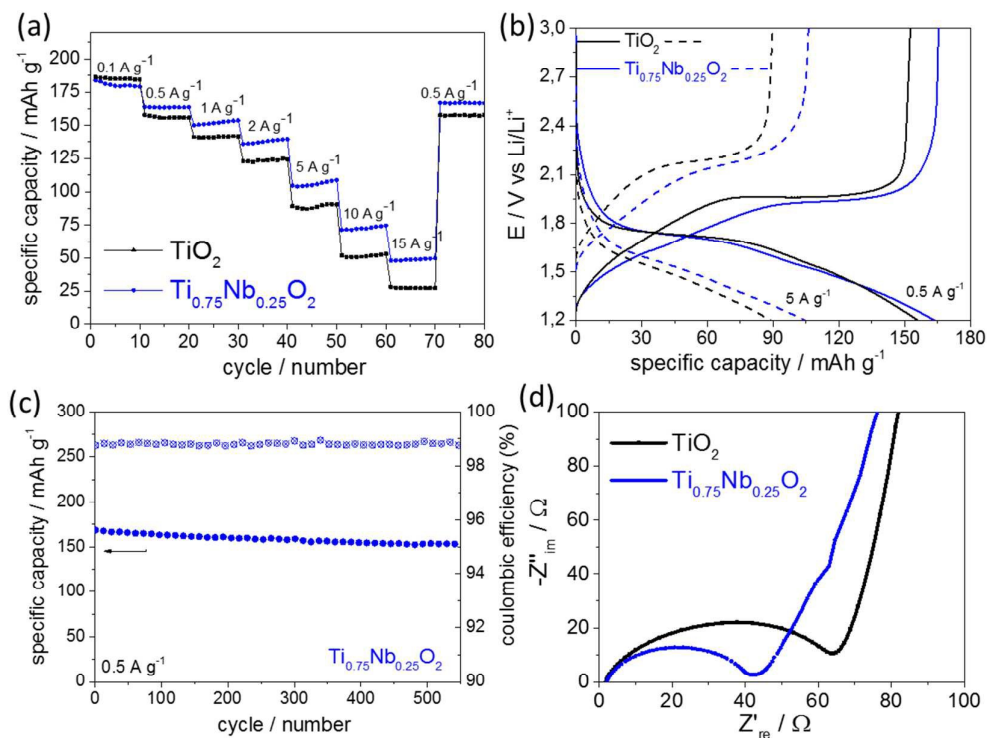


Figure 5: (a) Electrochemical performance plots of specific capacity (mAh g^{-1}) versus cycle number at different nominal C rates for TiO_2 (squares, black) and $\text{Ti}_{0.75}\text{Nb}_{0.25}\text{O}_2$ (circles, blue) at applied currents in the range of 0.1 to 15 A g^{-1} (10 cycles each). (b) Charge/discharge profile for TiO_2 and $\text{Ti}_{0.75}\text{Nb}_{0.25}\text{O}_2$, showing the potential (vs Li/Li^+) versus specific capacity (mAh g^{-1}) at applied currents of 0.5 and 5 A g^{-1} , respectively. (c) Long term cycling stability study showing specific capacity (left y-axis) and the coulombic efficiency (right y-axis) versus the cycle number (applied current of 0.5 A g^{-1}). (d) Electrochemical impedance spectra of coin half cells based on TiO_2 and $\text{Ti}_{0.75}\text{Nb}_{0.25}\text{O}_2$ electrodes versus Li/Li^+ .

Table of Contents entry

Highly Pseudocapacitive Nb-doped TiO₂ High Power Anodes for Lithium-ion BatteriesMechthild Lübke^a, Juhun Shin^a, Peter Marchand^a, Dan Brett^b, Paul Shearing^b, Zhaolin Liu^cand Jawwad A. Darr^{a*}